

Experimental observation of stress formation during selective laser melting using in situ X-ray diffraction

Felix Schmeiser^a, Erwin Krohmer^b, Norbert Schell^c, Eckart Uhlmann^b, Walter Reimers^a

^a*Institute for Materials Science and Technology, Metallic Materials, Technische Universität Berlin, Ernst-Reuter-Platz 1, 10587 Berlin, Germany*

^b*Institute for Machine Tools and Factory Management, Technische Universität Berlin, Pascalstraße 8-9, 10587 Berlin, Germany*

^c*Helmholtz-Zentrum Geesthacht, Max-Planck-Str. 1, 21502 Geesthacht, Germany*

Corresponding author: Felix Schmeiser, felix.schmeiser@tu-berlin.de

Abstract

Despite the ongoing success of metal additive manufacturing and especially the selective laser melting (SLM) technology, process-related defects, distortions and residual stresses impede its usability for fracture-critical applications. In this paper, results of in situ X-ray diffraction experiments are presented that offer insights into the strain and stress formation during the manufacturing of multi-layer thin walls made from Inconel 625. Using different measuring modes and laser scanning parameters, several experimental observations are discussed to validate and extend theoretical models and simulations from the literature. As a sample is built-up layer by layer, the stress state changes continuously up until the last exposure. The localized energy input leads to a complex stress field around the heat source that involves alternating tensile and compressive stresses. The correlation of temperature and yield strength results in a stress maximum at a certain distance to the top layer. The present study demonstrates the potential of high-energy synchrotron radiation diffraction for in situ SLM research.

Keywords:

- Selective laser melting
- In situ
- High energy synchrotron radiation diffraction
- Stress formation
- Inconel 625

1 Introduction

Selective laser melting (SLM), also known as laser powder bed fusion (LPBF), is a powder bed based additive manufacturing technique with the capability to produce parts with complex geometry while maintaining good mechanical properties. Though the market of SLM systems has been growing rapidly in the last years [1], process-inherent variations in part quality and mechanical properties inhibit the use of SLM-produced parts in fracture-critical applications [2]. This is particularly due to residual stresses [3,4] and crack-inducing defects [4] in the produced parts, which have a negative effect on fatigue strength. In order to solve process-related quality variations, a profound understanding of the formation of defects and residual stresses is necessary.

During the manufacturing process, a thin layer of metal powder is melted locally by a focused laser beam, then solidifies and bonds with the already solidified layers beneath. After the spreading of a new powder layer, the laser beam scans again and the cycle is iterated until the part is completed. The SLM process leads to a complex thermal regime in the part as the temperature distribution varies rapidly with time and location during manufacturing [5]. As a layer is exposed, the laser energy is focused on a very small spot size, with a typical laser spot diameter of $d_L = 50 \mu\text{m}$ to $200 \mu\text{m}$ [6], which leads to a rapid heating of the exposed area. The metal powder is molten, then solidifies rapidly while the heat is dissipated into the surrounding volume. At the same time, the laser scan continues and heats the adjacent area so that a track is formed, which again necessitates the dissipation of heat energy.

The numerous repetitions of this procedure on continuously changing positions result in steep temperature gradients. Previously exposed layers are also affected by this and experience cyclic heating and cooling, all of which affects the microstructure of the part, its mechanical properties and the stress state during and after production. During production, as the part is built up layer by layer, heat accumulates in certain areas of the part caused by the increasing distance to the substrate plate and the poor heat conduction in the surrounding metal powder [7]. This adds another thermal boundary condition to be considered.

The phenomena described here, the highly focused heat source, the cyclic heating and cooling as well as the heat accumulation lead to a complex stress development in the part, which was described by Mercelis and Kruth [8]. During the formation of the current topmost layer, its contraction upon cooling is hindered by the underlying material, which leads to tensile stresses in the top layer. As more and more layers are built on top of it, these tensile stresses turn into compressive stresses that balance the tensile stresses of the above layers. The temperature gradient mechanism (TGM) describes the phenomenon of the development of compressive stresses surrounding the laser spot due to high temperature gradients. The residual stresses generated during the SLM process can reach the yield strength of the material [8] and generally lead to undesired behavior such as distortion, cracking and

early onset fatigue [9–11]. Controlling the stress state by optimizing the process parameters necessitates knowledge of the fundamental physical mechanisms.

Stress measurements have been performed with several methods on different geometries and process parameters. Researchers have used neutron diffraction [12–14], X-ray diffraction [14–16] and synchrotron radiation diffraction [14,17] experiments or mechanical testing [18–20] to determine the residual stress state of parts created via SLM. However, the temporal history of the temperature distribution has a crucial role in the generation of residual stresses [21] and cannot be investigated by ex situ measurements. Controlling the thermal regime during the process is the key to improve the properties of the part. Some modern SLM systems feature melt-pool monitoring and thermal imaging systems to detect hot spots and potential defects during the process [22]. These techniques deliver valuable data about the surface of the part. To gather information about the inner conditions of the part, simulations are a useful tool. Due to the complex heat distribution, simulating the moving heat source and its impact on the underlying material is associated with some uncertainties. Therefore, the simulations have to be validated experimentally.

In situ measurements on bulk properties in general have been scarce, with X-ray imaging techniques emerging only recently. Several research groups have performed X-ray imaging experiments observing melt pool dynamics, pore formation and powder scattering [23–34] in the SLM process. Other experiments provided insights in powder recoating dynamics [35,36] and surface smoothing by laser remelting [37]. Furthermore, the feasibility of in situ X-ray diffraction during SLM was demonstrated [33,34]. However, a comprehensive study of the stress buildup in SLM parts via in situ diffraction is yet to be presented in the literature. The metrological prerequisites to capture the SLM process with good temporal resolution have emerged only in recent years. The latest improvements in synchrotron radiation sources generate highly brilliant radiation and new, fast detectors enable quick image acquisition and high spatial resolutions simultaneously.

To perform such in situ experiments, a custom-built SLM machine is necessary, preferably close to an industrial standard system. Up until now, all presented in situ studies were focused on single track or single layer measurements. For the experiments presented here, a custom-built process chamber based on an industrial standard SLM system is utilized [38]. It allows for in situ X-ray transmission experiments featuring an automated powder recoating system with adjustable layer thickness, a moveable building platform and part geometries up to $70 \times 3 \times 10 \text{ mm}^3$. This machine is capable of fabricating multi-layer samples automatically while simultaneously the synchrotron radiation beam is irradiating a specific, desired gauge volume anywhere in the sample before, during and after laser exposure. Using this machine, Wide Angle X-ray Scattering (WAXS) experiments were performed at the HEMS-beamline P07 at PETRA-III (DESY, Hamburg, Germany) and 2D diffraction patterns were analyzed to gather unprecedented experimental insights on the buildup of strains and stresses in samples made of the Nickel base alloy Inconel 625.

2 Materials and methods

2.1 Modified selective laser melting system

The SLM system used in the experiments is a modified AconityMINI from Aconity3D GmbH (Herzogenrath, Germany) with a custom-built process chamber developed and built at Technische Universität Berlin. The laser system consists of a continuous wave Ytterbium fiber laser YLR-400-AC from IPG Laser GmbH (Burbach, Germany), which emits radiation at a wavelength of $\lambda = 1070$ nm with a nominal power output of 400 W. The laser fiber is connected to a 3-axis deflection unit Axialscan-30 from Raylase GmbH (Wessling, Germany) via a collimator. Through the deflection unit, the laser beam with a focus diameter of about 60 μm in a working distance of 445 mm is directed onto a powder bed with a size of $70 \times 3 \times 10$ mm (length \times width \times height). The powder bed is limited by a replaceable S355J2 steel substrate on the bottom and two glassy carbon plates, supplied by HTW Hochtemperatur-Werkstoffe GmbH (Thierhaupten, Germany), with a thickness of 1 mm in X-ray transmission direction each. The funnel-based fully automatic powder recoating mechanism and an adjustable layer thickness enable the buildup of samples with a maximum height of 10 mm.

Before each experiment, a new steel substrate was mounted on the sample holder and sandwiched between the glassy carbon plates. Then, the first powder layer was deposited as thinly as possible and checked visually to assure bonding of the melted layer on the substrate. The process chamber was sealed and purged with argon gas until an oxygen level below 2000 ppm was reached. Throughout every experiment, the oxygen content at powder bed level was monitored. In addition, the argon gas atmosphere was circulated by the installed circulation pump and filtered continuously in order to remove welding fumes from the laser beam path. The sample holder was positioned in transverse direction depending on the desired position of the X-ray gauge volume. Inlet and outlet windows of the process chamber for synchrotron radiation are made of Kapton foils (DuPont, Wilmington USA), with a thickness of 50 μm . Consequently, the synchrotron radiation beam passes through ambient air, Kapton foils, argon and glassy carbon, besides the desired Inconel 625 sample, with overall negligible noise.

In order to keep the boundary conditions concerning the heat flow close to the industrial process, the samples were produced with a maximum thickness of 2.5 mm in transmission direction. Hence, between sample and glassy carbon, a powder barrier with a thickness of about 0.25 mm on both sides was established. Since the thermal conductivity of solidified Inconel 625 is at least one order of magnitude higher than thermal conductivity of Inconel 625 powder [39,40], heat conduction occurs primarily through the solidified parts of the sample. Taking into account simulative results on heat transfer in the formation of melt tracks with steel powder [41], it is derived that the powder barrier in the experiments adequately mimics heat transfer conditions of the conventional SLM process.

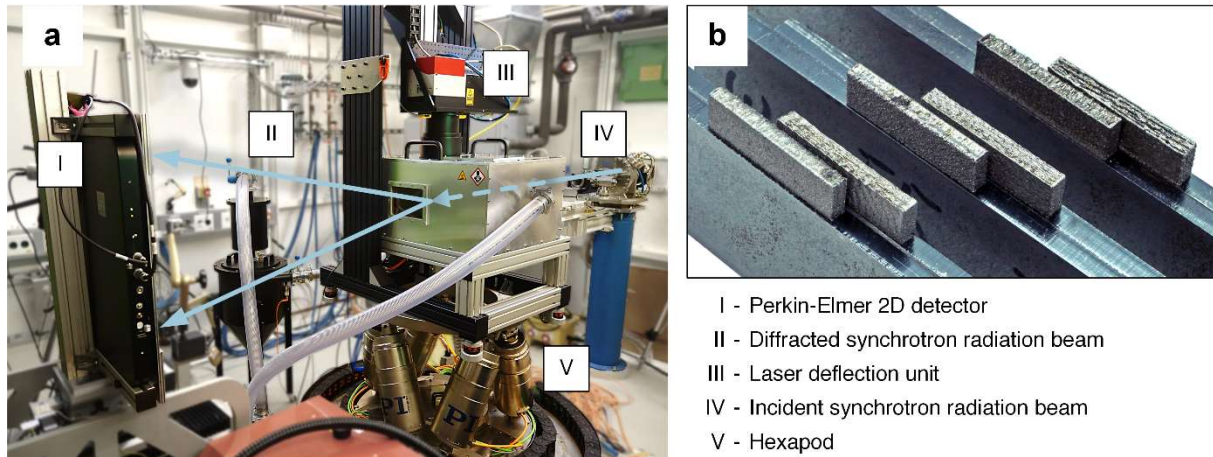


Figure 1 a) Experimental Setup at PETRA-III P07 EH3 (DESY, Hamburg, Germany) and b) Example parts that were built using the custom SLM system. From left to right: $P_L = 275$ W, L-scan and T-scan. $P_L = 165$ W, L-scan and T-scan. $P_L = 55$ W, L-scan and T-scan. Part geometry $20 \times 5 \times 2.5$ mm³. Parts are built upon steel substrates.

2.2 Materials

The samples were built using an Inconel 625 (UNS N06625/W.Nr. 2.4856) metal powder supplied by m4p materials solutions GmbH (Magdeburg, Germany). The particle size ranged from 20 to 63 μm according to the manufacturer. The metal powder has a nominal chemical composition of 20.7 wt% Cr, 8.4 wt% Mo, 0.6 wt% Si, 0.4 wt% Mn, 3.5 wt% Nb and 0.5 wt% Fe.

2.3 Experimental procedure

The SLM process in general is adjusted and optimized via a large range of parameters [42] with estimations of more than 130 parameters affecting part quality [43]. In the experiments presented here, the number of variables was reduced to both simplify the manufacturing process as much as possible and to highlight the basic mechanisms at work. Furthermore, a simple geometry was chosen for the samples. Thin walls with dimensions of $20 \times 5 \times 2.5$ mm³ were manufactured using different sets of parameters, see **Figure 1b**.

The laser scanning pattern was identified as one of the drivers of thermal management and therefore stress generation [44]. Industrial SLM systems employ various scanning strategies in one part to ensure a good surface finish as well as little to no porosity. To create a smooth finish, the contour of a part is scanned with a different set of laser parameters than the ‘filling’. For the diffraction experiments in transmission mode, this would result in irradiating a gauge volume made up of scanned tracks in different directions and with different scanning parameters. This impedes interpretation and complicates the attribution of phenomena to a specific set of parameters. Therefore, no contour scans were employed in the manufacturing of the samples presented here. Furthermore, only unidirectional scanning patterns without meandering were used. Two resulting scanning patterns were investigated and consequently named ‘longitudinal scanning’ (L-scan) and ‘transversal scanning’ (T-scan) following the orientation of the scanning vectors in relation to the incident synchrotron radiation beam, see **Figure 2**.

The second parameter that was varied is the energy input, i.e. laser power P_L and scanning speed v_L . Three sets of scanning parameters were used and are shown in **Table 1**. A laser power of $P_L = 275$ W and the corresponding scanning speed of $v_L = 760$ mm/s (set 1) represents an industrial standard parameter set that ensures high density parts. Set 3 features the lowest acceptable laser power that still leads to $\sim 99.5\%$ relative density, as was found in preliminary tests. The low scanning speed of $v_L = 50$ mm/s in turn led to good temporal resolution and a favorable data-to-noise ratio. Set 2 was chosen as an intermediary energy input between the two extremes.

In combination with the two scanning strategies, a total of six sets of parameters were investigated. The other manufacturing parameters were kept constant. Major ones are also presented in **Table 1**.

In **Figure 2**, the experimental procedure concerning the measuring positions is illustrated. For each set, three samples with varying measuring positions were built. Furthermore, two measurement modes were employed. Most of the samples were observed using measurement mode 1 (MM1). In this

Table 1 Sample parameters. a) Laser parameter sets b) Scanning patterns c) Process parameters that were kept constant for all samples.

a)	Laser power P_L [W]	Scanning speed v_L [mm/s]	c) Constant process parameters	
Set 1	275	760	Layer thickness Δz	50 μm
Set 2	165	456	No. of layers	100
Set 3	55	50	Hatch distance h	120 μm
b)	Hatch length [mm]	No. of hatches	Laser spot diameter d_L	~ 60 μm
L-Scan	2.28	168	Jump speed v_j	1000 mm/s
T-Scan	19.8	20	Sample geometry	$20 \times 5 \times 2.5$ mm ³

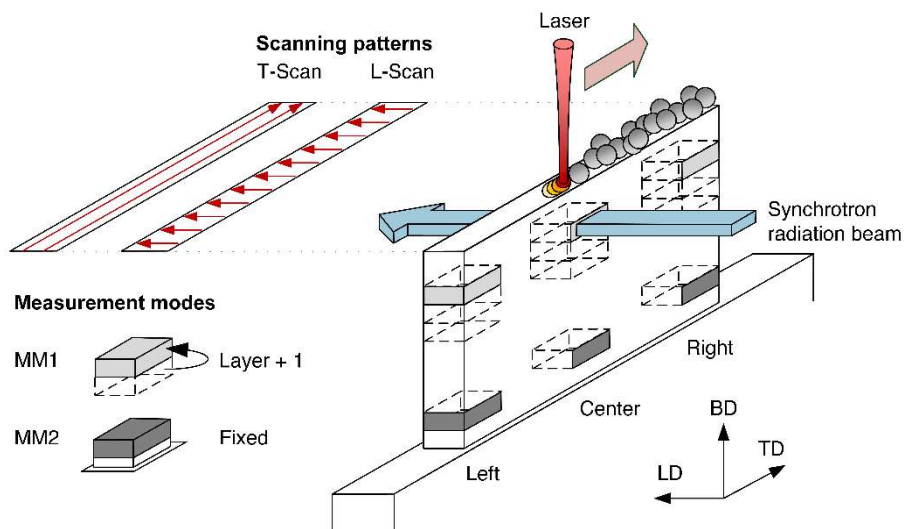


Figure 2 Experimental Procedure. Measurement Mode 1 (MM1) - Gauge volume in fixed distance to top layer. Measurement Mode 2 (MM2) - Gauge volume in fixed height. Schematic representations of scanning patterns evaluated. For the T-scan, the hatching direction is oriented along LD, while for the L-scan, the hatching direction is oriented along TD.

configuration, the gauge volume changes from layer to layer and stays in a fixed distance of 150 μm to the top layer. On the other hand, the gauge volume in measurement mode 2 (MM2) stays in a fixed position during the whole process. Furthermore, the three major axes are illustrated in **Figure 2**. The longitudinal direction (LD) and the transversal direction (TD) span the working plane of the laser on the powder bed, with the longitudinal direction referring to the beam direction of the incident synchrotron radiation beam. The building direction (BD) is perpendicular to the working plane and refers to the sample height direction.

2.4 In situ high energy synchrotron X-ray diffraction

The in situ diffraction experiments were performed at the HEMS P07 beamline at DESY (Hamburg, Germany) [45] using an energy of $E = 98.02 \text{ keV}$ ($\lambda = 0.12649 \text{ \AA}$). An X-ray beam size of $750 \times 70 \mu\text{m}^2$ was chosen. This enabled good spatial resolution in build direction. The width of the beam was set accordingly to ensure enough grains being irradiated so that full diffraction patterns could be collected. A schematic setup of both the experiment and the data analysis is shown in **Figure 3**.

The modified process chamber was set up on the heavy-duty hexapod provided by Helmholtz-Zentrum Geesthacht. In **Figure 1a**, the setup in the experimental hutch at the beamline is shown. The distance between sample and detector was 1521.147 mm to capture full Debye-Scherrer rings of the first five (hkl) reflections. Lanthanum hexaboride (LaB_6) was used to determine the sample-to-detector distance, see supplementary section 6.2. The Perkin-Elmer XRD1621 detector was used with an exposure time of $t = 0.1 \text{ s}$ and a frame rate of $f = 10 \text{ Hz}$. Maximum intensity ranged from 100 to 300 counts depending on the reflection chosen. In supplementary **Figure 11**, a comparison of a powder sample diffraction pattern and an in situ measurement of solidified material is shown.

The diffraction patterns were segmented into cake pieces and integrated using Fit2D [46] to gather 1D-2 θ -profiles from the 2D diffraction patterns. The 1D profiles were batch-processed using custom Python scripts that featured the ‘lmfit’ package [47]. A Voigt function was used to fit the experimental data and determine the peak position, full-width half maximum (FWHM) and integrated intensity of the (311) reflection. As mentioned in section 2.1, there was a powder barrier between the glassy carbon plates and the sample, which was irradiated as well. As the powder barrier is thin compared to the solidified material, contributing to $\sim 13\%$ of irradiated mass, its diffracted intensity is much lower than the bulk material. Unlike the bulk material, the powder does not experience mechanical stresses that induce peak shifts in the diffraction patterns. The superposition of unstressed powder with low diffracted intensity and stressed bulk material with a high diffracted intensity produces asymmetric peaks, which reduce the accuracy of the fitting function. To account for the powder layer, thus only

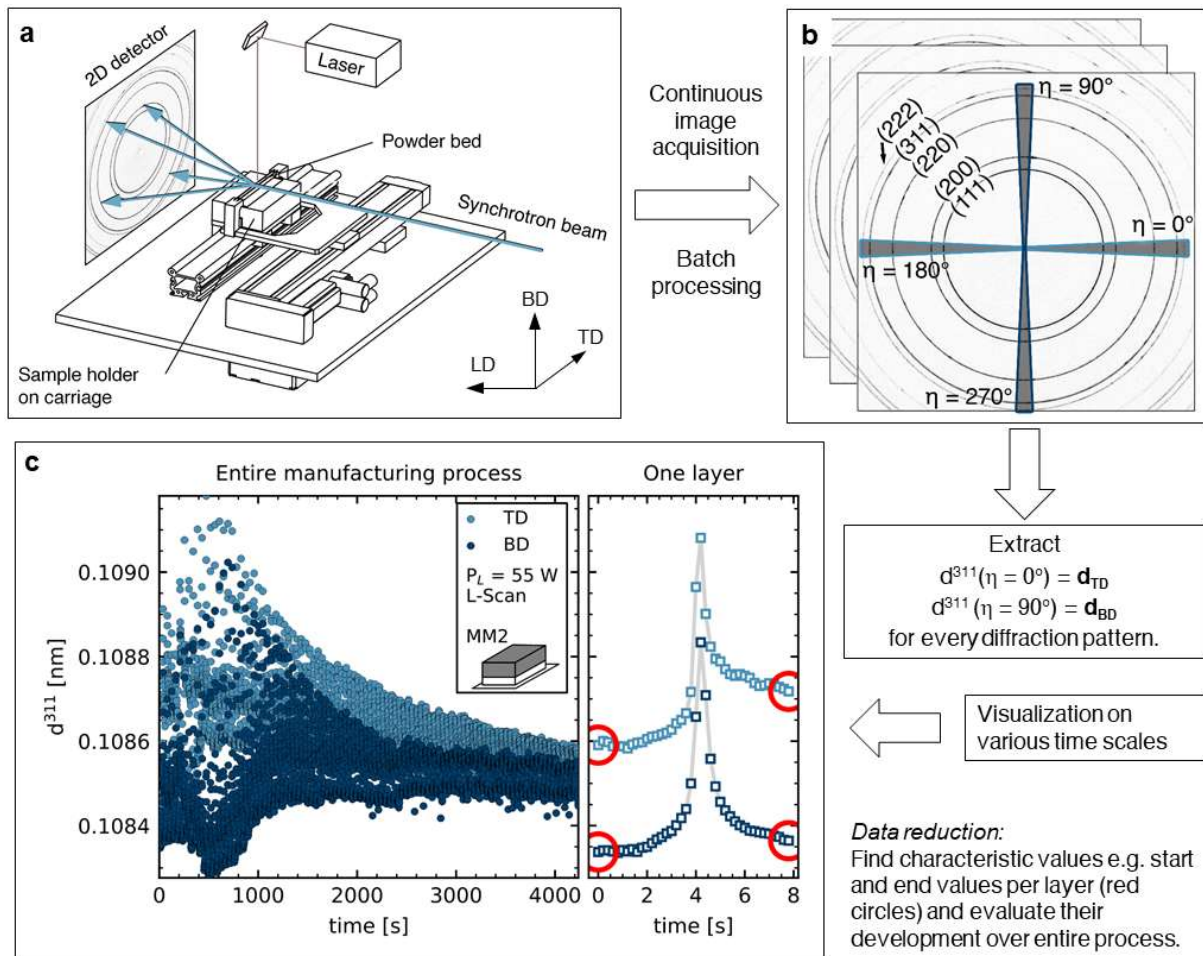


Figure 3 Schematic data generation and evaluation process: a) Experimental setup with relevant direction denotations, b) Example diffraction pattern and analyzed directions and c) Illustrative data visualizations of a sample manufactured using a laser power of $P_L = 55$ W and L-scan in MM2 with the gauge volume in the center of the 5th layer of the sample. The red circles mark the data points that have been extracted for all layers and subsequently plotted to generate **Figure 4**.

the top 60% of the peak data was used for the peak fitting. This way, the diffracted intensity of the powder barrier and the resulting asymmetry was filtered out and did not distort the subsequent analysis.

2.5 Strain free lattice parameter

The strain free lattice parameter is dependent of the chemical composition and crystallographic structure of the material. Wang et al. showed that the chemical composition of Inconel 625 processed via SLM can actually change as the part is being built up [48]. This in turn alters the strain free lattice parameter. To verify if this was the case in our samples as well, wavelength-dispersive X-ray spectroscopy (WDX) measurements were performed on the TD-BD plane of the specimen at ZELMI, Technische Universität Berlin. One sample per set of parameters, six in total, was investigated.

Seven alloy elements were analyzed: Ni, Cr, Mo, Nb, Fe, Si and Mn and a circular spot size of $d = 20 \mu\text{m}$ was used. To investigate potential concentration gradients in both TD and BD, line scans

with a step size of 500 μm , ranging from the lower edge of the part to the top edge were performed in three locations, i.e. left edge, center and right edge. The substrate was cut off for this investigation.

Contrary to Wang et al., our samples showed no concentration gradients of the alloy elements – neither over the height (BD) of the sample nor its length (TD). While there was a standard deviation of 0.25 to 0.29 wt% of chromium, the most volatile alloy element, for each line scan, the changes in concentration over the sample height and width were stochastic and did not follow any monotonous trends.

Comparing the gauge volume of WDX, 20 μm in diameter, to the one used for the in situ WAXS measurements, $750 \times 70 \times 2500 \mu\text{m}^3$, the diffraction measurements average over a much larger volume. Therefore, the strain free lattice parameter is unsusceptible to the slight local differences in composition shown by WDX. As no compositional gradients emerged from our measurements, a single d_0 is proposed to be sufficient to characterize the whole sample.

To determine d_0 , small cuboids with an edge length of 700 μm were cut out of the parts using micro electrical discharge machining (EDM) for subsequent diffraction experiments. Opening the aperture to $1 \times 1 \text{ mm}^2$, this sample size enabled ‘bathing’ the cuboids in the synchrotron radiation beam so that all cuboid surfaces were irradiated. By irradiating the whole volume of the specimen, a stress-free state can be assumed considering the force and moment equilibrium. The strain free lattice parameter can therefore be calculated from the peak position.

Additionally, the d_0 -measurements were performed in a DHS1100 furnace from Anton Paar GmbH (Graz, Austria) to assess the temperature dependence of d_0 for temperatures up to $T = 800 \text{ }^\circ\text{C}$, which was found to be linear for all of the samples investigated, see supplementary **Figure 14**.

2.6 Strain and stress analysis

Using the d_0 measurements, the lattice spacings were converted into strains following

$$\varepsilon^{311} = \frac{d^{311} - d_0^{311}}{d_0^{311}}. \quad (1)$$

This was done for the two assumed principal directions of stress, TD and BD, see analogous procedures for the calculation of asymmetric strains in high pressure research [49]. To prevent a beam center error, the lattice spacings extracted from two opposing cake pieces were averaged as illustrated in **Figure 3**. Hence, d_{TD} is calculated by averaging the lattice parameter at $\eta = 0^\circ$ and $\eta = 180^\circ$, the lattice parameter in building direction d_{BD} by averaging $\eta = 90^\circ$ and $\eta = 270^\circ$. The strains calculated this way are the sum of the elastic and the thermal component, though. Without knowledge of the exact temperature, the purely elastic component cannot be determined. Since d_0 itself is temperature-dependent, the calculation of absolute strains is not possible. Therefore, the absolute strain values given in the plots are not discussed further, as they are arbitrarily based on a constant, temperature-

independent d_0 . Nevertheless, the visualization of the directional strains is a valuable tool to detect differences in trends between TD and BD.

On the other hand, the strain difference between TD and BD is calculated as

$$\varepsilon_{TD-BD}^{311} = \frac{d_{TD}^{311} - d_{BD}^{311}}{d_0^{311}}. \quad (2)$$

Because both lattice parameters are calculated from the same diffraction pattern and gauge volume, any difference between the two cannot be due to a difference in temperature and is therefore purely elastic. Furthermore, the temperature-dependence of d_0 has a negligible effect on the strain difference. From the strain difference ε_{TD-BD} , the stress difference can be calculated with equation (3),

$$\sigma_{TD} - \sigma_{BD} = \frac{E^{311}}{(1 + \nu^{311})(1 - 2\nu^{311})} [(1 - \nu^{311})(\varepsilon_{TD} - \varepsilon_{BD}) + \nu^{311}(\varepsilon_{BD} - \varepsilon_{TD})] \quad (3)$$

which was derived from Hauk et al. [50] The temperature-dependence of the elastic constants was extrapolated from the single crystal constants presented by Wang et al. [51]. In supplementary section 6.4 the relevant data is presented. The coefficient of thermal expansion was calculated from the experimental data described in the section 2.5. It is shown in supplementary **Figure 14**. In this way, the stress difference was determined for a number of different temperatures. Temperature gradients in the gauge volume cannot be resolved. Due to the gauge volume's geometry, the temperature gradients are more pronounced in TD than in BD, therefore leading to a higher uncertainty of the stress values in TD.

However, the lattice spacings for TD and BD are extracted from the same diffraction pattern from the same gauge volume. They are therefore affected by the temperature gradients in the same magnitude. Thus, the uncertainty of the lattice spacings in TD and BD is the same and mostly dependent on the fitting uncertainty of the raw data, which was negligible in our case.

3 Results

3.1 Influence of heat input on strains

One of the key origins of stresses during SLM are the thermal gradients inherent to the process [8]. During the manufacturing process, the heat distribution changes continuously. To demonstrate this, it is suitable to investigate the development of certain strain values over the course of production.

One example is shown in **Figure 4**. The data is derived from three samples, which were built using the same set of parameters, i.e. L-scan and a laser power of $P_L = 55$ W, while respectively observing the three measuring positions, i.e. left edge, center and right edge, of the sample. The experiments were performed in MM1. In **Figure 4**, the data points represent the strain values at the start and at the end of each layer for all layers over the course of manufacturing, whereby 'layer' means during exposure and laser-metal-interaction, see **Figure 3**.

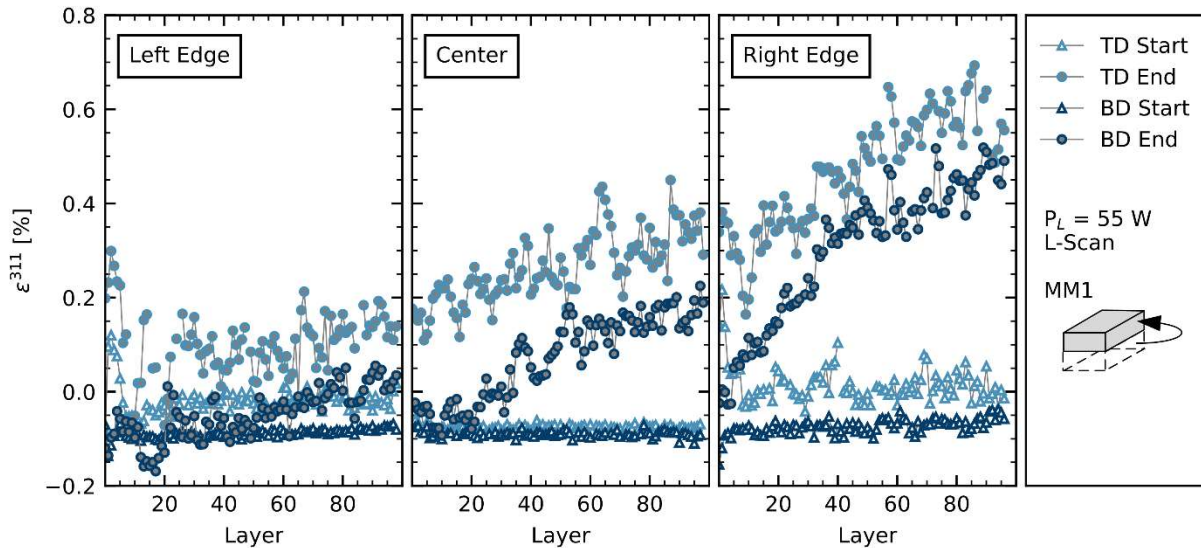


Figure 4 Strain progression for TD (light blue) and BD (dark blue). Triangular markers show the first strain value measured in the gauge volume for that layer after the laser was turned on, circle markers show last strain value of that layer before the laser was turned off.

The first strain value for each layer delivers information about the strain state after recoating and subsequent cooling of the sample. Then, during the production of one layer, the laser passes over the gauge volume and leads to a sharp increase in the strains. After the laser passage, the gauge volume cools again, but the strains stay elevated, which is mirrored by the last strain value for each layer. For each of the measuring positions, the start values stay relatively constant for all layers, but there are distinct trends in the progression of the end values over the course of the manufacturing process.

The constant values at the start of each layer can be explained with the inter-layer dwell time due to recoating. After the previous layer has been fully exposed, the sample is coated again with a new powder layer. The recoating process takes about 15 s. During this time interval, the whole sample and therefore the gauge volume cools down. Therefore, the temperature and the strain state are constant at the beginning of each layer. At the end of one layer, the gauge volume is obviously hotter than in the beginning, which explains the difference between start and end values in one layer. As more layers are built, the top surface of the sample and accordingly the gauge volume increases its distance from the substrate, which serves as a heatsink. As the distance rises, the heat transfer away from the heat source and the gauge volume is hindered by heat accumulation. Therefore, the end strain values increase with an increasing number of layers.

The L-scan utilized for these samples illuminates another effect, which is heat accumulation in lateral direction from left to right, which is in accordance with simulative results from Parry et al. [52]. The graphs for the end values get much steeper from left to right. The gauge volume in the left measuring position is exposed right at the start of each new layer when the sample in total has cooled due to the coating procedure. This allows for a fast heat transfer away from the gauge volume and results in moderately constant end values for each layer. The gauge volume on the right side of the sample is

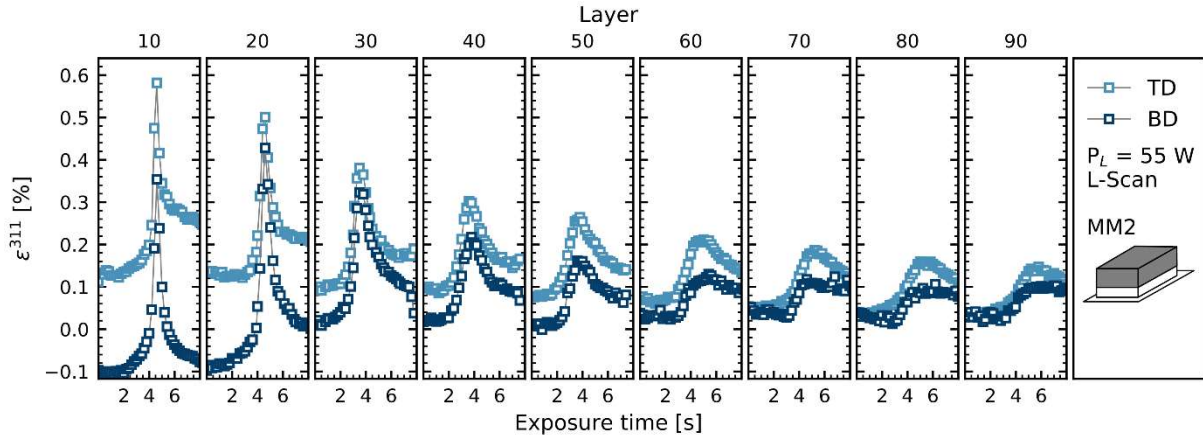


Figure 5 Strain progression in MM2, measuring position in the center of the sample. Each subplot shows the progression for one layer. The gauge volume was placed in the 5th layer, so the first subplot shows the strain progression with 5 additional layers above the gauge volume; in the second subplot, 15 layers are above the gauge volume and so on. The data points marked in light blue show the strains in TD, dark blue ones show BD.

exposed in the end of each layer. At the point that the laser passes over the gauge volume, about 95% of the sample has already been exposed and therefore heated significantly. This inhibits the heat transport away from the gauge volume and leads to a sort of lingering heat, which in turn results in a steep increase in the end strain values.

While **Figure 4** shows the values for a moving gauge volume (MM1) and thus delivers information about the upper region of the sample, **Figure 5** demonstrates the impact of the laser in the lower region of the sample. The figure shows the strain progression in a fixed gauge volume (MM2) placed in the 5th layer of the sample. Each subplot shows the strains at a point where a specific number of layers has been processed, yet the gauge volume stays in the 5th layer.

A number of observations can be supported by this figure. Each laser passage over the gauge volume influences the strain state, regardless of the gauge volume's distance to the heat source. This figure illustrates that the laser has an impact on the strain state of the first layers until the very end of the manufacturing process, despite there being about 4.5 mm of material above the gauge volume. While the strains in TD and BD converge over time, the laser passage still leads to a visible peak in the strains. At the same time, the laser does not have the same effect on both directions. The strains in TD are affected more, resulting in a higher peak there.

The occurrence of a peak is expected as a result of the heat flow from the top layer during exposure, which in turn leads to thermal expansion throughout the sample. On the other hand, the difference in peak height is surprising and cannot be attributed to temperature. Instead, it is proposed that tensile stresses are induced in TD. The lower peak in BD is a reaction to the tensile stresses in TD and a result of transverse contraction due to the constant volume boundary condition. As the laser scans the top layer, the thermal expansion in BD is uninhibited due to the free surface at the top. In TD on the other hand, the surrounding material acts as a fixation, so that the thermal expansion of the top portion of the

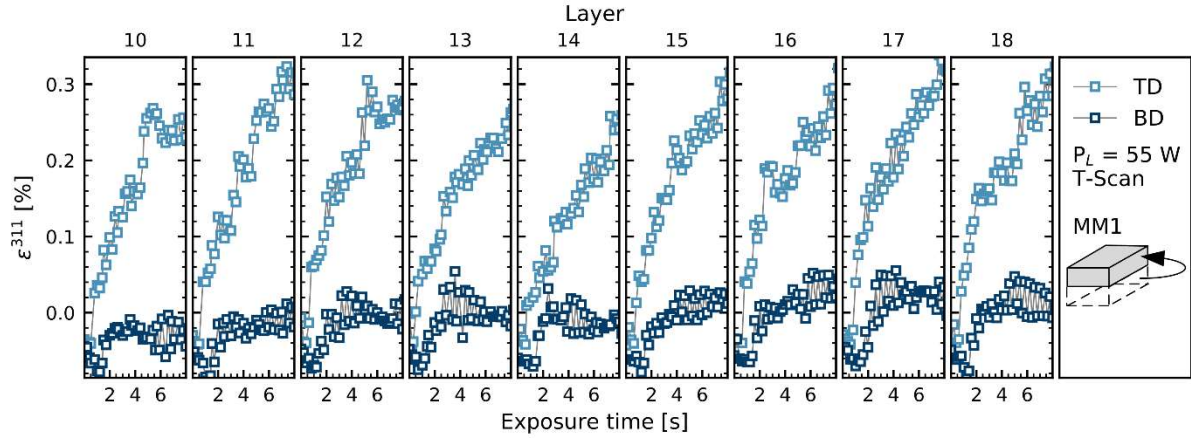


Figure 6 Strain Progression in MM1, measuring position in the center of the sample. Each subplot shows progression for one layer. The data points marked in light blue show the strains in TD, dark blue ones show BD.

sample induces tensile stresses in the gauge volume, which leads to the peak visible in the figure.

After the laser has passed, the strains in TD and BD converge again at a higher strain point than at the beginning of the layer. This demonstrates that the strain state in the observed gauge volume is altered by the laser up to the last layer.

The transverse contraction hypothesis is also supported by the T-scan experiments. In **Figure 6**, the strain progression for nine consecutive layers in a T-scan sample is shown. The strains in TD form a steep slope in each layer. This is caused by the uniform heating of the gauge volume via the T-scan. In contrast to the L-scan, here the laser passes over the gauge volume about 20 times in total during the exposure of a single layer. Therefore, the gauge volume heats more uniformly than in the L-scan, where a visible peak is formed as seen in **Figure 5**. The increase in temperature leads to a rise of the lattice strains, as visible in TD. In BD on the other hand, the slope is minimal and for some of the layers displayed in the figure, e.g. for layer 10 and 14, the values even stay constant at $\varepsilon^{311} = 0\%$. Therefore, the increase in lattice strain due to thermal expansion has to be counteracted and compensated by a different mechanism. As discussed earlier, tensile stresses are induced in the gauge volume in TD due to hindered contraction. These lead to a further increase in lattice strains in TD. As a result of these tensile stresses, a transverse contraction is induced in BD. The transverse contraction offsets the thermal expansion so that the net lattice strain is close to zero percent.

3.2 In-plane stresses and out-of-plane stresses

So far, results referring to the influence of temperature and heat distribution on the strain state have been described using the in situ measurements. The next step is the validation of existing models for stress formation during the SLM process.

As mentioned in section 2.3, BD is the direction perpendicular to the working plane and therefore characterizes out-of-plane stresses. The working plane is defined by LD and TD. Therefore, in-plane stresses are characterized by TD as the experimental data delivers no information in LD.

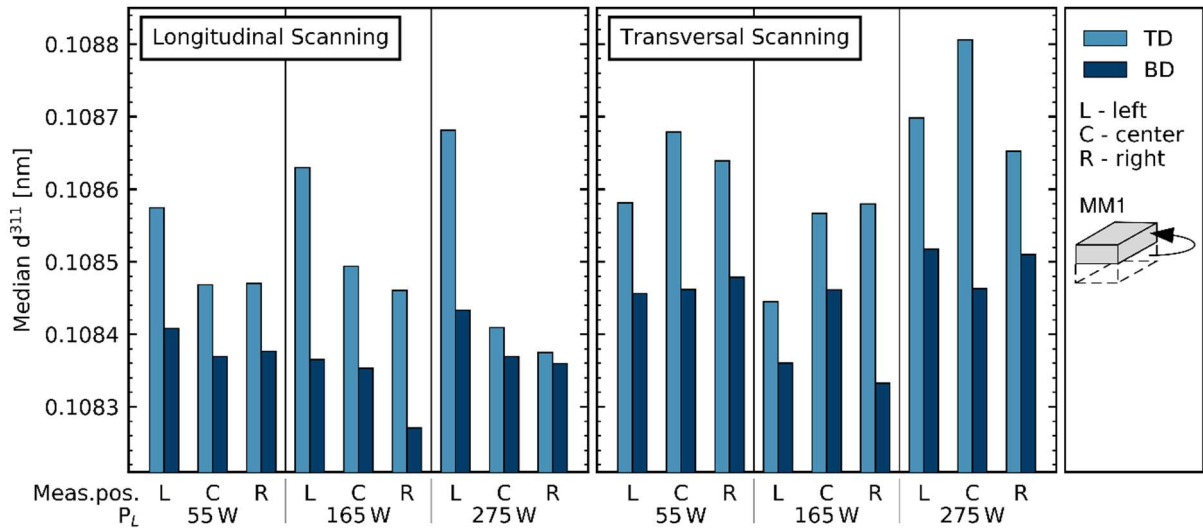


Figure 7 Median d^{311} values over the whole process sorted by process parameters. Light blue bars represent the median lattice spacing in TD and dark blue bars in BD. For all sets of process parameters, the median lattice spacing in TD is larger than in BD.

In all of the experiments using MM1, the lattice spacings in TD were larger than in BD. This is demonstrated in **Figure 7**, which shows the median lattice spacings for all sets of parameters. This effect is a result of the cooling of the top layer. The solidified material shrinks as it cools. The underlying, colder material inhibits the contraction, which induces compressive stresses in TD in the top layer and tensile stresses in TD in the underlying material. In response, the tensile stresses cause a transverse contraction in BD. These two mechanisms lead to the difference in the median lattice spacings, shown in **Figure 7**. Because the temperature in the gauge volume and therefore for TD and BD is the same, the difference has to be explained as a stress effect.

In the literature, divergent results have been presented. Bass et al. found that the stresses in build direction were larger than the in-plane stresses on the outside of their cylindrical parts, but smaller closer to the center of the part [53]. Nadammal et al. on the other hand reported stress distributions that were similar in TD and BD in both the middle of their part as well as the edge [54]. Our experiments show that during the manufacturing process, the stresses are higher in TD than BD in all of the examined measuring positions. In layers with increased distance to the top, the findings might be different and are subject to further investigations.

3.3 Thermal gradient mechanism

In 2006, Mercelis and Kruth proposed the thermal gradient mechanism (TGM) as one of the driving factors in the generation of residual stresses during SLM [8]. They argue that the rapid heating by the laser beam leads to steep temperature gradients. As the material's strength drops due to the increase in temperature, it expands for the same reason. The expansion is hindered by the colder material below and thus, compressive stresses are induced in the hot material. These compressive stresses caused by the laser can be observed in the experiments presented here.

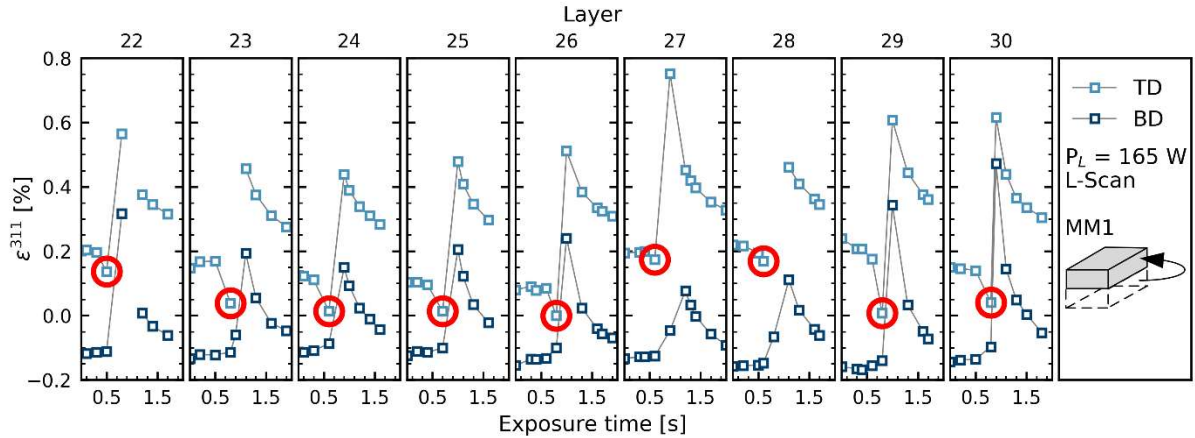


Figure 8 Strain progression MM1, measuring position at left edge of the sample. The data points marked in light blue show the strains in TD, dark blue ones show BD. Red circles mark the minimum strain value in TD for each layer. Low data density and missing values are caused by the high laser scanning velocity of $v_L = 456$ mm/s and an unfavorable data-to-noise ratio.

Figure 8 shows the strain progression in a section of nine layers for a sample that was scanned longitudinally with a laser power of $P_L = 165$ W. This sample showed local minimal strain values in TD right before the strain peak in 76 out of 100 layers. The minimal values are marked with red circles. The drop occurs as the laser approaches the gauge volume. Therefore, the gauge volume is heated up, which should result in an increase in strains due to thermal expansion. Right before the laser passes the gauge volume, the compressive stress field induced by the laser and described by Mercelis and Kruth counteracts the thermal expansion to a degree that shows up as an actual drop in strains. Mercelis and Kruth do not distinguish between in-plane and out-of-plane stresses in their model, though. Following their argument, the drop in strains should be visible in both directions, which it is not. This might be caused by the proximity of the gauge volume to the top layer. Perhaps a strain decrease in BD would be visible in a gauge volume further below the top layer. If both the mechanical and thermal boundaries of our experimental setup are incorporated into the model by Mercelis and Kruth, an additional stress-inducing mechanism is possibly present here.

The gauge volume is fixed in the center of the sample. During the L-scan, the laser scan is headed from left to right. Right before the laser passes over the gauge volume, the part of the sample that is left of the gauge volume is very hot while the rest of the sample is at a low temperature, see supplementary **Figure 12** for reference. There is a temperature gradient in both TD and BD, though. The material's response in BD can be imagined as that of a cantilever beam in this scenario, because there is a free surface that permits uninhibited thermal expansion while the substrate acts as the fixed end. TD on the other hand can be pictured as a beam that is fixed on both sides due to the material bonding to the substrate. The fixed beam is heated on one side. Before any heat flow can occur, the heated part expands due to thermal expansion. Because the beam is fixed on both ends, the other side, where the gauge volume is located, has to be compressed. This difference between BD, free end, and TD, fixed on both ends, causes the drop in lattice spacing to occur only in TD.

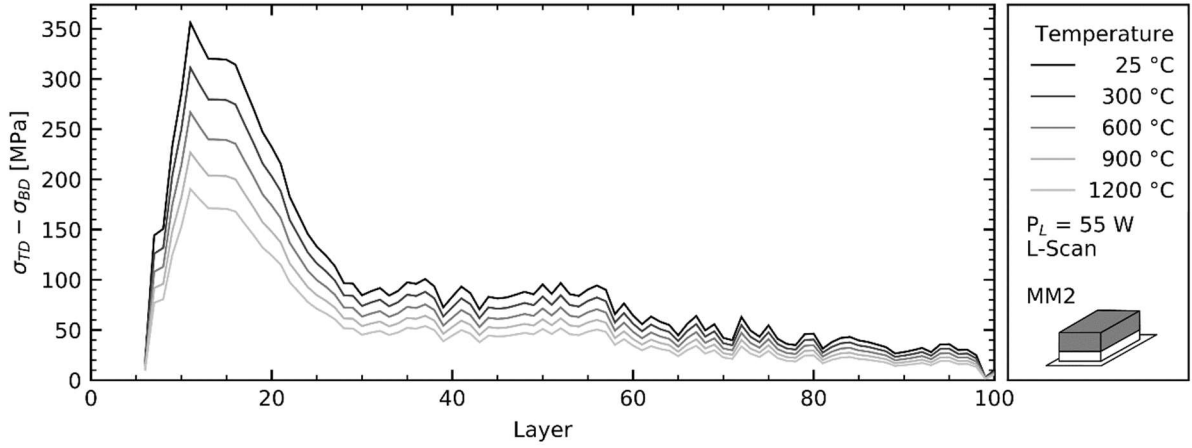


Figure 9 Layer-wise median stress difference $\sigma_{TD} - \sigma_{BD}$ for complete manufacturing process in MM2 with the gauge volume placed in the center of the 5th layer of the sample. Different shades of grey correspond to different temperatures. The median stress difference was calculated from the median strain difference per layer.

3.4 Thermally induced stress maximum

The magnitude of thermally induced stresses varies during the process depending on the distance of the observed volume to the heat source. To illustrate this, the median stress difference for each layer is calculated and shown in **Figure 9**. At this point, the utilized custom-built SLM system does not feature a temperature measuring device. Since the mechanical properties and the strain-free lattice parameter change with temperature, the stress progression is shown for a range of temperatures from room temperature up to $T = 1200$ °C. Regardless of the exact temperature of the gauge volume, there is a noticeable trend in the stress progression.

Up until layer 11, the median stress difference is increasing in every layer. Since the stress difference between TD and BD is analyzed instead of absolute stresses in either direction, it is not possible to distinguish between tensile and compressive stresses in the individual directions. Nevertheless, in conjunction with the results described earlier, it seems plausible that a combination of a maximum in tensile stresses in TD and a resulting maximum transverse contraction in BD lead to the observed maximum in stress difference. The data shows that the stress difference reaches a maximum about 300 μm below the top layer and the heat source. After that, the stress differences decrease and converge to almost zero. This does not mean that the directional stresses are equal to zero, but the stress anisotropy is greatly reduced.

In the first data points in **Figure 9**, the gauge volume is located directly below the top layer. Here, the temperature of the gauge volume is very high, therefore leading to a significant reduction in the material's yield strength σ_y . Due to the reduced strength of the material, the magnitude of stresses resulting from the hindered contraction described earlier is limited. As more layers are built, the gauge volume's temperature decreases, which in turn results in an increase in yield strength σ_y . The material, now being colder and having higher strength, can endure higher elastic stresses, which leads to the maximum in stress difference visible in the plot. After reaching the maximum, the impact of the

hindered contraction in the top layer on the gauge volume diminishes, leading to a reduction of the stress difference until it eventually converges to zero. The repeated laser scans with each layer act as a stress-relieving heat treatment, thereby further reducing the stress anisotropy.

For subsequent investigations, MM2 will be used at varying layer counts to investigate whether the appearance of the maximum stress difference changes over the course of production or whether it is constantly to be found about 300 μm below the top surface.

3.5 Stress fields in the heat affected zone

The results presented in the previous sections illustrate the generation of stresses during the SLM process in various ways. By combining these results, a schematic depiction of the heat affected zone (HAZ) surrounding the laser spot was developed. The HAZ encompasses varying stress fields caused by the heating and cooling of the material, which were observed in the various experiments discussed here. In **Figure 10**, a qualitative illustration of the HAZ is shown. Furthermore, the strain progression for a single layer representative of all of the following effects is given to show the corresponding data points.

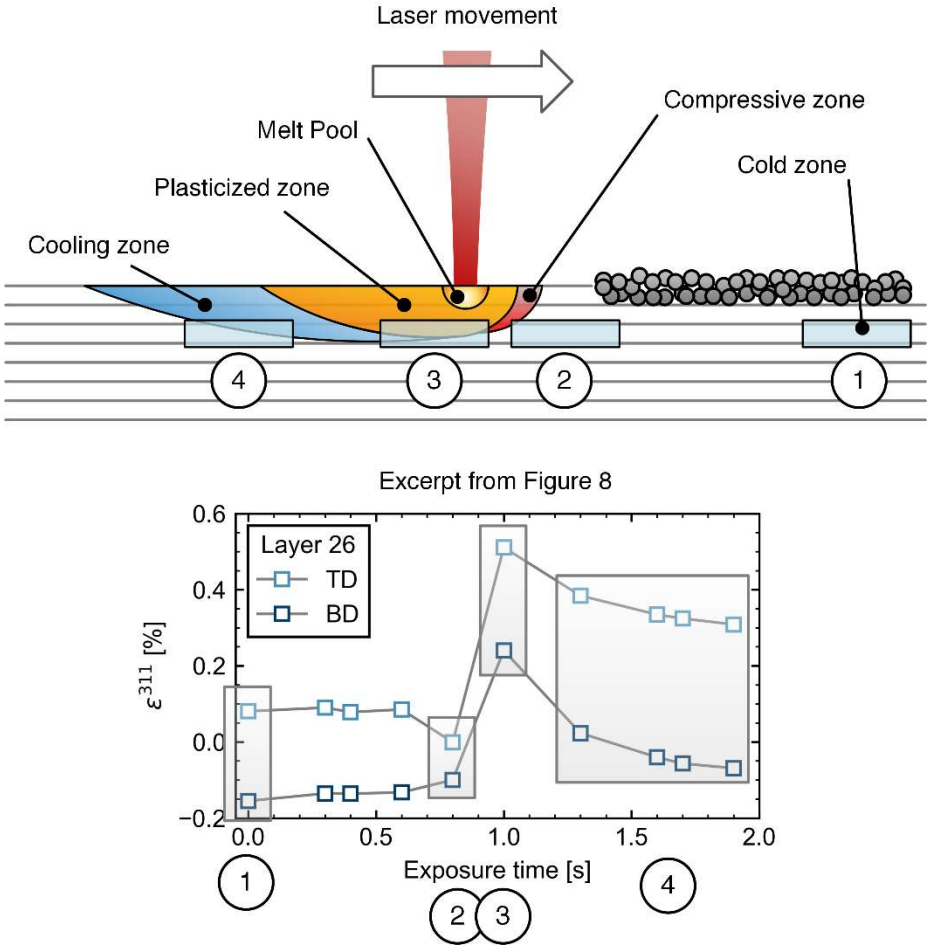


Figure 10 Model of the HAZ, its stress fields and the corresponding data points observed during the in situ measurements. Top: Schematic representation of the HAZ. Bottom: Strain progression during a single layer, excerpt from **Figure 8**.

The HAZ consists of the melt pool, a plasticized zone around the melt pool, the cooling zone trailing the laser spot and a compressive zone, which was first described in the present study.

During the exposure of a single layer, the strain progression in a fixed gauge volume can be segmented into four distinct zones. In both zone 1 (cold zone) and zone 4 (cooling zone) the TGM causes the strain difference. During the exposure of the previous layer, the material in zone 1 was exposed and plasticized. Due to the high temperature, the associated low strength and the hindered expansion, the material was compressed plastically. Then, after being exposed by the laser, the material cooled down. At this point, the shrinkage was hindered by the underlying material. The hindered contraction has a much higher impact in-plane of the layer (TD) than out-of-plane (BD). Therefore, the tensile stresses described by the TGM are induced in TD. Subsequently, BD is compressed due to transverse contraction, thusly explaining that the strains in TD are generally higher than in BD.

The analogous process happens in zone 4. After the exposure by the laser at $t = 1.0$ s, the material cools down and experiences the same stress inversion as zone 1 in the previous layer, resulting in high strains in TD due to tensile stresses and lower strains in BD as a result of transverse contraction. As shown in section 3.4, the magnitude of this effect changes with the vertical distance between the laser spot and the gauge volume.

In zone 2 (compression zone) a new effect not previously observed is at play. The thermal conduction is slower than the reaction of the material to heat. Therefore, the HAZ expands rapidly while zone 2 is still cold and therefore, with respect to **Figure 10**, compressed by the incoming hot material on the left.

The position of the gauge volume relative to the heat-affected zone (HAZ) around the laser is of great importance. Due to the extremely high heating and cooling rates of up to 10^6 K/s during cooling as investigated by Bertoli et al. [55], some of the effects are only observable in very specific locations.

4 Conclusions

Utilizing a custom-built SLM system, the first comprehensive in situ diffraction experiments were performed for this emerging manufacturing process at the P07 HEMS beamline at DESY. Different measurement modes were employed that allowed both tracking a single, fixed gauge volume in the sample and fixing the gauge volume relative to the top surface. Several thermal phenomena during the SLM process were shown experimentally, including lateral heat accumulation in a single layer as well as vertical heat accumulation in build direction. Furthermore, the results provide insights in a number of stress-related phenomena during laser-metal interaction. In-plane strains were found to be generally higher than out-of-plane strains, with tensile stresses in TD resulting in a transverse contraction in BD. The localized heat input induces a complex stress field that involves an outer halo of compressive stresses, which was experimentally detected in TD. Furthermore, the TGM model was confirmed and

a mechanism that clarifies directional differences in the emerging stress field was introduced. During the SLM process, the stress state of the sample is altered by the laser up to the very last layer. A maximum stress difference between in-plane and out-of-plane stresses was found about 300 μm below the top layer when using the L-scan, a laser power of $P_L = 55 \text{ W}$ and a scanning speed of $v_L = 50 \text{ mm/s}$.

For the first time, the strain and stress development during the manufacturing of SLM parts was investigated using in situ X-ray diffraction. The presented results prove the feasibility of in situ diffraction experiments for multi-layer samples in SLM based on a custom-built process chamber for an industrial scale machine. In situ diffraction experiments offer remarkable and promising insights into the strain and stress development as presented in this study. Furthermore, in future, the 2D diffraction data will yield significant findings regarding texture development and, when using different materials, phase transformations during the process.

5 Acknowledgements

This research is based on the project DFG RE 688/73-1, UH 100/207-1 respectively, which is kindly supported by the Deutsche Forschungsgemeinschaft (DFG). The authors acknowledge Helmholtz-Zentrum-Geesthacht for the provision of laboratory facilities, various SLM system accessories and experimental support. The authors acknowledge Helmholtz-Zentrum-Berlin for the provision of laboratory equipment and ZELMI at Technische Universität Berlin for the WDX measurements. Finally, the authors thank Alexander Poeche, Amadeus Pauer, Bettina Camin, Emad Mawaad, Francisca Cemerika, Henry Angerstein, Jan Rosigkeit, Jonas Schmidt, Mateus Dobecki, Matthias Schelhorn, Thomas Braun and Wilhelm Schulze for their support conducting the in situ diffraction experiments.

References

- [1] T. Wohlers, I. Campbell, O. Diegel, J. Kowen, Wohlers Report 2018: 3D printing and additive manufacturing state of the industry, WOHLERS Associates, Fort Collins, 2018.
- [2] M. Seifi, A. Salem, J. Beuth, O. Harrysson, J.J. Lewandowski, Overview of Materials Qualification Needs for Metal Additive Manufacturing, JOM 68 (2016) 747–764. <https://doi.org/10.1007/s11837-015-1810-0>.
- [3] S. Leuders, M. Thöne, A. Riemer, T. Niendorf, T. Tröster, H.A. Richard, H.J. Maier, On the mechanical behaviour of titanium alloy TiAl6V4 manufactured by selective laser melting: Fatigue resistance and crack growth performance, Int. J. Fatigue 48 (2013) 300–307. <https://doi.org/10.1016/j.ijfatigue.2012.11.011>.
- [4] U. Zerbst, K. Hilgenberg, Damage development and damage tolerance of structures manufactured by selective laser melting – a review, Procedia Struct. Integrity 7 (2017) 141–148. <https://doi.org/10.1016/j.prostr.2017.11.071>.
- [5] M.J. Ansari, D.-S. Nguyen, H.S. Park, Investigation of SLM Process in Terms of Temperature Distribution and Melting Pool Size: Modeling and Experimental Approaches, Materials (Basel) 12 (2019). <https://doi.org/10.3390/ma12081272>.

- [6] S. Ly, A.M. Rubenchik, S.A. Khairallah, G. Guss, M.J. Matthews, Metal vapor micro-jet controls material redistribution in laser powder bed fusion additive manufacturing, *Sci. Rep.* 7 (2017) 4085. <https://doi.org/10.1038/s41598-017-04237-z>.
- [7] T. Mukherjee, H.L. Wei, A. De, T. DebRoy, Heat and fluid flow in additive manufacturing – Part II: Powder bed fusion of stainless steel, and titanium, nickel and aluminum base alloys, *Comput. Mater. Sci.* 150 (2018) 369–380. <https://doi.org/10.1016/j.commatsci.2018.04.027>.
- [8] P. Mercelis, J.-P. Kruth, Residual stresses in selective laser sintering and selective laser melting, *Rapid Prototyp. J.* 12 (2006) 254–265. <https://doi.org/10.1108/13552540610707013>.
- [9] V. Cain, L. Thijs, J. van Humbeeck, B. van Hooreweder, R. Knutsen, Crack propagation and fracture toughness of Ti6Al4V alloy produced by selective laser melting, *Addit. Manuf.* 5 (2015) 68–76. <https://doi.org/10.1016/j.addma.2014.12.006>.
- [10] J.-P. Kruth, J. Deckers, E. Yasa, R. Wauthlé, Assessing and comparing influencing factors of residual stresses in selective laser melting using a novel analysis method, *Proceedings of the Institution of Mechanical Engineers, Part B: Journal of Engineering Manufacture* 226 (2012) 980–991. <https://doi.org/10.1177/0954405412437085>.
- [11] B. Cheng, S. Shrestha, K. Chou, Stress and deformation evaluations of scanning strategy effect in selective laser melting, *Addit. Manuf.* 12 (2016) 240–251. <https://doi.org/10.1016/j.addma.2016.05.007>.
- [12] M.F. Zaeh, G. Branner, Investigations on residual stresses and deformations in selective laser melting, *Prod. Eng. Res. Devel.* 4 (2010) 35–45. <https://doi.org/10.1007/s11740-009-0192-y>.
- [13] M. Masoomi, N. Shamsaei, R.A. Winholtz, J.L. Milner, T. Gnäupel-Herold, A. Elwany, M. Mahmoudi, S.M. Thompson, Residual stress measurements via neutron diffraction of additive manufactured stainless steel 17-4 PH, *Data Brief* 13 (2017) 408–414. <https://doi.org/10.1016/j.dib.2017.06.027>.
- [14] A. Kromm, S. Cabeza, T. Mishurova, N. Nadammal, T. Thiede, G. Bruno, Residual Stresses in Selective Laser Melted Samples of a Nickel Based Superalloy, in: *Residual Stresses 2018*, Materials Research Forum LLC, 2018, pp. 259–264.
- [15] I. Yadroitsev, I. Yadroitsava, Evaluation of residual stress in stainless steel 316L and Ti6Al4V samples produced by selective laser melting, *Virtual Phys Prototyp.* 10 (2015) 67–76. <https://doi.org/10.1080/17452759.2015.1026045>.
- [16] Y. Liu, Y. Yang, Di Wang, A study on the residual stress during selective laser melting (SLM) of metallic powder, *Int J Adv Manuf Technol* 87 (2016) 647–656. <https://doi.org/10.1007/s00170-016-8466-y>.
- [17] T. Mishurova, K. Artzt, J. Haubrich, G. Requena, G. Bruno, Exploring the Correlation between Subsurface Residual Stresses and Manufacturing Parameters in Laser Powder Bed Fused Ti-6Al-4V, *Metals* 9 (2019) 261. <https://doi.org/10.3390/met9020261>.
- [18] C. Casavola, S.L. Campanelli, C. Pappalettere, Preliminary investigation on distribution of residual stress generated by the selective laser melting process, *J. Strain. Anal. Eng.* 44 (2009) 93–104. <https://doi.org/10.1243/03093247JSA464>.
- [19] M. Shiomi, K. Osakada, K. Nakamura, T. Yamashita, F. Abe, Residual Stress within Metallic Model Made by Selective Laser Melting Process, *CIRP Annals* 53 (2004) 195–198. [https://doi.org/10.1016/S0007-8506\(07\)60677-5](https://doi.org/10.1016/S0007-8506(07)60677-5).
- [20] B. Vrancken, V. Cain, R. Knutsen, J. van Humbeeck, Residual stress via the contour method in compact tension specimens produced via selective laser melting, *Scr. Mater.* 87 (2014) 29–32. <https://doi.org/10.1016/j.scriptamat.2014.05.016>.
- [21] M. Mani, B.M. Lane, M.A. Donmez, S.C. Feng, S.P. Moylan, A review on measurement science needs for real-time control of additive manufacturing metal powder bed fusion processes, *Int. J. Prod. Res.* 55 (2017) 1400–1418. <https://doi.org/10.1080/00207543.2016.1223378>.
- [22] S.K. Everton, M. Hirsch, P. Stravroulakis, R.K. Leach, A.T. Clare, Review of in-situ process monitoring and in-situ metrology for metal additive manufacturing, *Mater. Des.* 95 (2016) 431–445. <https://doi.org/10.1016/j.matdes.2016.01.099>.

- [23] A. Bobel, L.G. Hector, I. Chelladurai, A.K. Sachdev, T. Brown, W.A. Poling, R. Kubic, B. Gould, C. Zhao, N. Parab, A. Greco, T. Sun, In situ synchrotron X-ray imaging of 4140 steel laser powder bed fusion, *Materialia* 6 (2019) 100306. <https://doi.org/10.1016/j.mtla.2019.100306>.
- [24] R. Cunningham, C. Zhao, N. Parab, C. Kantzos, J. Pauza, K. Fezzaa, T. Sun, A.D. Rollett, Keyhole threshold and morphology in laser melting revealed by ultrahigh-speed x-ray imaging, *Science* 363 (2019) 849–852. <https://doi.org/10.1126/science.aav4687>.
- [25] C.L.A. Leung, S. Marussi, R.C. Atwood, M. Towrie, P.J. Withers, P.D. Lee, In situ X-ray imaging of defect and molten pool dynamics in laser additive manufacturing, *Nat Commun.* 9 (2018) 1355. <https://doi.org/10.1038/s41467-018-03734-7>.
- [26] C.L.A. Leung, S. Marussi, M. Towrie, R.C. Atwood, P.J. Withers, P.D. Lee, The effect of powder oxidation on defect formation in laser additive manufacturing, *Acta Mater.* 166 (2019) 294–305. <https://doi.org/10.1016/j.actamat.2018.12.027>.
- [27] C.L.A. Leung, S. Marussi, M. Towrie, J. del Val Garcia, R.C. Atwood, A.J. Bodey, J.R. Jones, P.J. Withers, P.D. Lee, Laser-matter interactions in additive manufacturing of stainless steel SS316L and 13-93 bioactive glass revealed by in situ X-ray imaging, *Addit. Manuf.* 24 (2018) 647–657. <https://doi.org/10.1016/j.addma.2018.08.025>.
- [28] A.A. Martin, N.P. Calta, J.A. Hammons, S.A. Khairallah, M.H. Nielsen, R.M. Shuttlesworth, N. Sinclair, M.J. Matthews, J.R. Jeffries, T.M. Willey, J.R.I. Lee, Ultrafast dynamics of laser-metal interactions in additive manufacturing alloys captured by in situ X-ray imaging, *Mater. Today Advances* 1 (2019) 100002. <https://doi.org/10.1016/j.mtadv.2019.01.001>.
- [29] A.A. Martin, N.P. Calta, S.A. Khairallah, J. Wang, P.J. Depond, A.Y. Fong, V. Thampy, G.M. Guss, A.M. Kiss, K.H. Stone, C.J. Tassone, J. Nelson Weker, M.F. Toney, T. van Buuren, M.J. Matthews, Dynamics of pore formation during laser powder bed fusion additive manufacturing, *Nat Commun.* 10 (2019) 1987. <https://doi.org/10.1038/s41467-019-10009-2>.
- [30] N.D. Parab, C. Zhao, R. Cunningham, L.I. Escano, K. Fezzaa, W. Everhart, A.D. Rollett, L. Chen, T. Sun, Ultrafast X-ray imaging of laser-metal additive manufacturing processes, *J. Synchrotron Radiat.* 25 (2018) 1467–1477. <https://doi.org/10.1107/S1600577518009554>.
- [31] N.D. Parab, C. Zhao, R. Cunningham, L.I. Escano, B. Gould, S. Wolff, Q. Guo, L. Xiong, C. Kantzos, J. Pauza, K. Fezzaa, A. Greco, A. Rollett, L. Chen, T. Sun, High-speed Synchrotron X-ray Imaging of Laser Powder Bed Fusion Process, *Synchrotron Radiat. News* 32 (2019) 4–8. <https://doi.org/10.1080/08940886.2019.1582280>.
- [32] Q. Guo, C. Zhao, L.I. Escano, Z. Young, L. Xiong, K. Fezzaa, W. Everhart, B. Brown, T. Sun, L. Chen, Transient dynamics of powder spattering in laser powder bed fusion additive manufacturing process revealed by in-situ high-speed high-energy x-ray imaging, *Acta Mater.* 151 (2018) 169–180. <https://doi.org/10.1016/j.actamat.2018.03.036>.
- [33] C. Zhao, K. Fezzaa, R.W. Cunningham, H. Wen, F. de Carlo, L. Chen, A.D. Rollett, T. Sun, Real-time monitoring of laser powder bed fusion process using high-speed X-ray imaging and diffraction, *Sci. Rep.* 7 (2017) 3602. <https://doi.org/10.1038/s41598-017-03761-2>.
- [34] N.P. Calta, J. Wang, A.M. Kiss, A.A. Martin, P.J. Depond, G.M. Guss, V. Thampy, A.Y. Fong, J.N. Weker, K.H. Stone, C.J. Tassone, M.J. Kramer, M.F. Toney, A. van Buuren, M.J. Matthews, An instrument for in situ time-resolved X-ray imaging and diffraction of laser powder bed fusion additive manufacturing processes, *Rev. Sci. Instrum.* 89 (2018) 55101. <https://doi.org/10.1063/1.5017236>.
- [35] L.I. Escano, N.D. Parab, L. Xiong, Q. Guo, C. Zhao, K. Fezzaa, W. Everhart, T. Sun, L. Chen, Revealing particle-scale powder spreading dynamics in powder-bed-based additive manufacturing process by high-speed x-ray imaging, *Sci. Rep.* 8 (2018) 15079. <https://doi.org/10.1038/s41598-018-33376-0>.
- [36] L.I. Escano, N.D. Parab, L. Xiong, Q. Guo, C. Zhao, T. Sun, L. Chen, Investigating Powder Spreading Dynamics in Additive Manufacturing Processes by In-situ High-speed X-ray Imaging, *Synchrotron Radiat. News* 32 (2019) 9–13. <https://doi.org/10.1080/08940886.2019.1582281>.

- [37] B. Richter, N. Blanke, C. Werner, N.D. Parab, T. Sun, F. Vollertsen, F.E. Pfefferkorn, High-speed X-ray investigation of melt dynamics during continuous-wave laser remelting of selective laser melted Co-Cr alloy, *CIRP Annals* (2019). <https://doi.org/10.1016/j.cirp.2019.04.110>.
- [38] E. Uhlmann, E. Krohmer, F. Hohlstein, W. Reimers, Development of an experimental test setup for in situ strain evaluation during selective laser melting, in: *Proceedings of the 28th Annual International Solid Freeform Fabrication Symposium*, Austin, Texas, 2017, pp. 1472–1480.
- [39] T. Özel, Y.M. Arisoy, L.E. Criales, Computational Simulation of Thermal and Spattering Phenomena and Microstructure in Selective Laser Melting of Inconel 625, *Phys. Procedia* 83 (2016) 1435–1443. <https://doi.org/10.1016/j.phpro.2016.08.149>.
- [40] L.C. Wei, L.E. Ehrlich, M.J. Powell-Palm, C. Montgomery, J. Beuth, J.A. Malen, Thermal conductivity of metal powders for powder bed additive manufacturing, *Addit. Manuf.* 21 (2018) 201–208. <https://doi.org/10.1016/j.addma.2018.02.002>.
- [41] I. Kovaleva, O. Kovalev, I. Smurov, Model of Heat and Mass Transfer in Random Packing Layer of Powder Particles in Selective Laser Melting, *Phys. Procedia* 56 (2014) 400–410. <https://doi.org/10.1016/j.phpro.2014.08.143>.
- [42] P. O'Regan, P. Prickett, R. Setchi, G. Hankins, N. Jones, Metal Based Additive Layer Manufacturing: Variations, Correlations and Process Control, *Procedia Comput. Sci.* 96 (2016) 216–224. <https://doi.org/10.1016/j.procs.2016.08.134>.
- [43] I. Yadroitsev, *Selective laser melting: Direct manufacturing of 3D-objects by selective laser melting of metal powders*, LAP Lambert Academic Publ, Saarbrücken, 2009.
- [44] J.L. Bartlett, X. Li, An overview of residual stresses in metal powder bed fusion, *Addit. Manuf.* 27 (2019) 131–149. <https://doi.org/10.1016/j.addma.2019.02.020>.
- [45] N. Schell, A. King, F. Beckmann, T. Fischer, M. Müller, A. Schreyer, The High Energy Materials Science Beamline (HEMS) at PETRA III, *MSF* 772 (2013) 57–61. <https://doi.org/10.4028/www.scientific.net/MSF.772.57>.
- [46] A.P. Hammersley, S.O. Svensson, M. Hanfland, A.N. Fitch, D. Hausermann, Two-dimensional detector software: From real detector to idealised image or two-theta scan, *High Pressure Research* 14 (1996) 235–248. <https://doi.org/10.1080/08957959608201408>.
- [47] M. Newville, T. Stensitzki, D.B. Allen, A. Ingargiola, LMFIT: Non-Linear Least-Square Minimization and Curve-Fitting for Python, Zenodo, 2014.
- [48] Z. Wang, E. Denlinger, P. Michaleris, A.D. Stoica, D. Ma, A.M. Beese, Residual stress mapping in Inconel 625 fabricated through additive manufacturing: Method for neutron diffraction measurements to validate thermomechanical model predictions, *Mater. Des.* 113 (2017) 169–177. <https://doi.org/10.1016/j.matdes.2016.10.003>.
- [49] A.K. Singh, The lattice strains in a specimen (cubic system) compressed nonhydrostatically in an opposed anvil device, *Journal of Applied Physics* 73 (1993) 4278–4286. <https://doi.org/10.1063/1.352809>.
- [50] V. Hauk, *Structural and Residual Stress Analysis by Nondestructive Methods*, Elsevier, 1997.
- [51] Z. Wang, A.D. Stoica, D. Ma, A.M. Beese, Diffraction and single-crystal elastic constants of Inconel 625 at room and elevated temperatures determined by neutron diffraction, *Mater. Sci. Eng. A* 674 (2016) 406–412. <https://doi.org/10.1016/j.msea.2016.08.010>.
- [52] L. Parry, I.A. Ashcroft, R.D. Wildman, Understanding the effect of laser scan strategy on residual stress in selective laser melting through thermo-mechanical simulation, *Addit. Manuf.* 12 (2016) 1–15. <https://doi.org/10.1016/j.addma.2016.05.014>.
- [53] L. Bass, J. Milner, T. Gnäupel-Herold, S. Moylan, Residual Stress in Additive Manufactured Nickel Alloy 625 Parts, *J. Manuf. Sci. Eng.* 140 (2018) 61004. <https://doi.org/10.1115/1.4039063>.
- [54] N. Nadammal, S. Cabeza, T. Mishurova, T. Thiede, A. Kromm, C. Seyfert, L. Farahbod, C. Haberland, J.A. Schneider, P.D. Portella, G. Bruno, Effect of hatch length on the development of microstructure, texture and residual stresses in selective laser melted superalloy Inconel 718, *Mater. Des.* 134 (2017) 139–150. <https://doi.org/10.1016/j.matdes.2017.08.049>.

- [55] U. Scipioni Bertoli, G. Guss, S. Wu, M.J. Matthews, J.M. Schoenung, In-situ characterization of laser-powder interaction and cooling rates through high-speed imaging of powder bed fusion additive manufacturing, *Mater. Des.* 135 (2017) 385–396.
<https://doi.org/10.1016/j.matdes.2017.09.044>.

1 6 Supplementary Information

2 6.1 Supplementary Figures

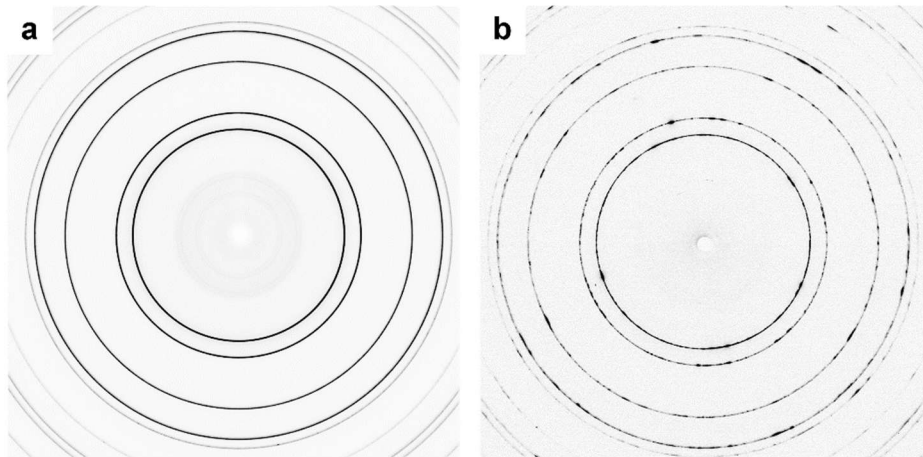


Figure 11 Example diffraction patterns of a) Inconel 625 powder measured ex situ and b) bulk Inconel 625 processed by SLM measured in situ. The powder diffraction pattern shows a uniform intensity distribution and perfectly circular rings, while the in situ measurement of solidified material shows an uneven intensity distribution, which indicates the growth of coarser grains and preferred orientations.

3

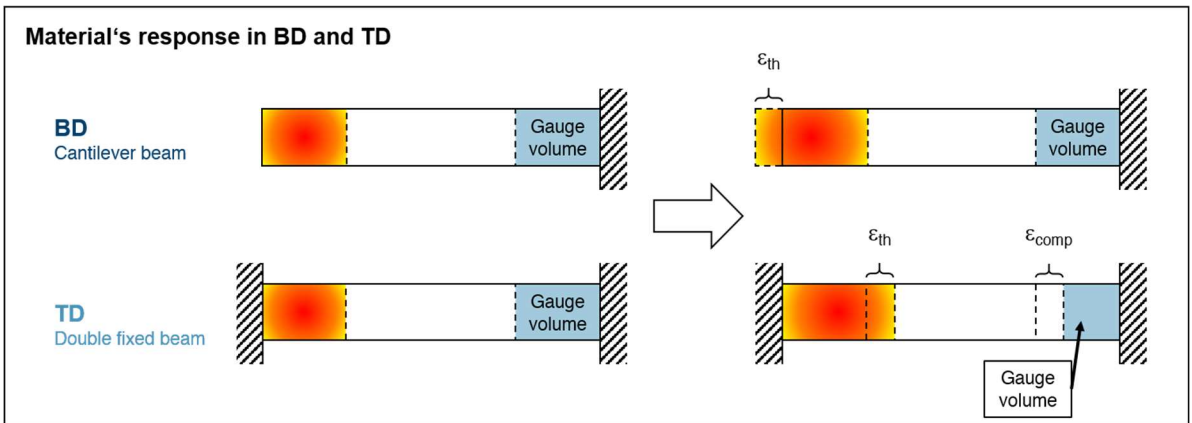
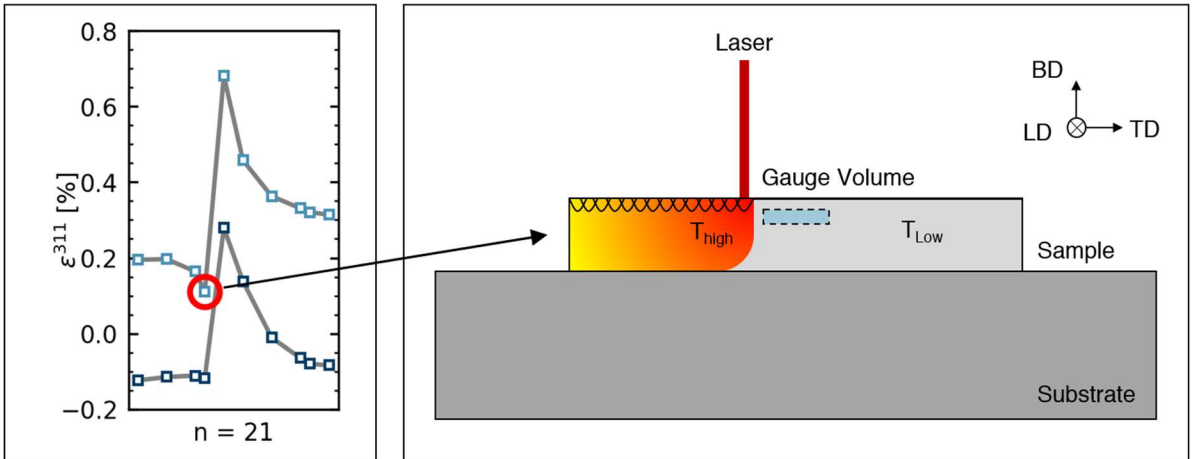
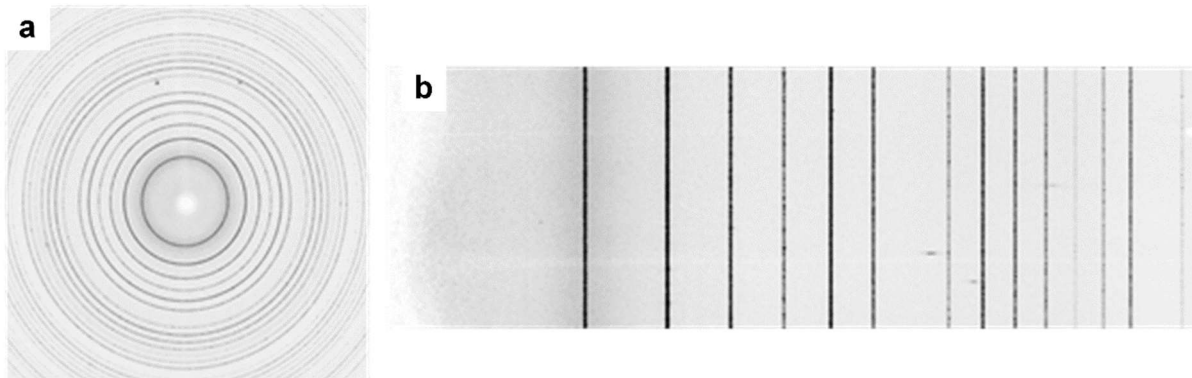


Figure 12 Model representation of material's response to approaching heated zone.

5 6.2 Calibration using LaB₆

6 LaB₆ powder is commonly used in diffraction experiments to calculate the sample-to-detector distance
7 and the detector tilt. To perform the calibration, the powder sample was fixated between the glassy
8 carbon plates in the process chamber in place of a sample. Diffraction patterns were acquired with the
9 same exposure parameters as during the in situ measurements. As a powder, LaB₆ is stress-free and
10 therefore shows perfectly circular diffraction rings. Since the lattice spacings of LaB₆ have been
11 determined very precisely in the past, the software Fit2D, which was used for the subsequent image
12 analysis, can determine the experimental parameters sample-to-detector distance and detector tilt by
13 fitting a number of Debye-Scherrer rings.

14 In **Figure 13a**, an example diffraction pattern of LaB₆ is shown. After calibration and full azimuthal
15 integration over 360°, the result is **Figure 13b**, where the vertical axis corresponds to the azimuthal
16 angle and the horizontal axis corresponds to the diffraction angle. There, it is clear to see that the
17 diffraction rings, projected as lines, are vertical and parallel, therefore the calibration was successful
18 and the subsequent image analysis of Inconel 625 diffraction patterns was correct.



19

20

21

Figure 13 LaB₆ powder diffraction pattern a) before calibration and b) after calibration and full azimuthal integration.

22

23 **6.3 Strain-free lattice parameter**

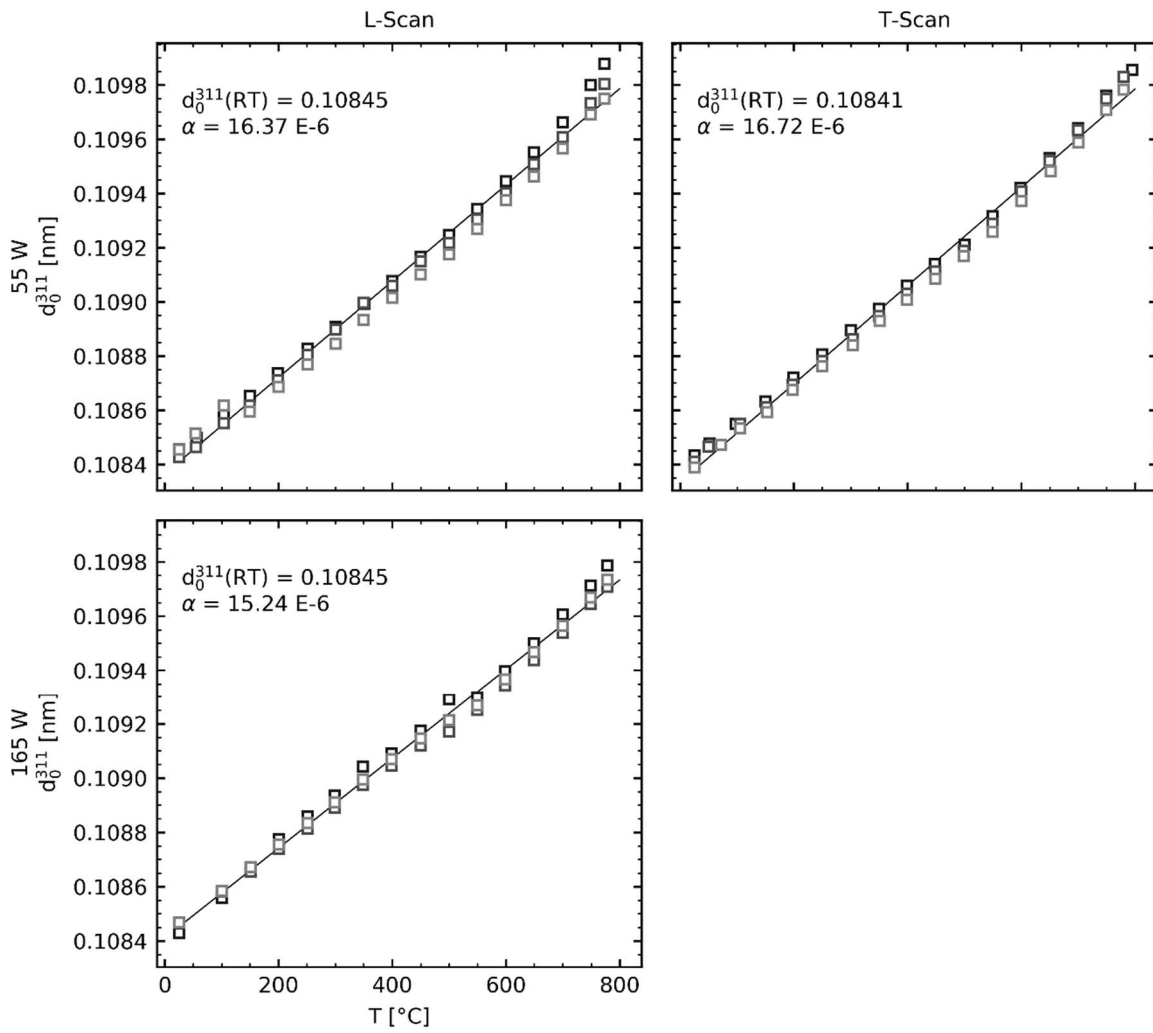
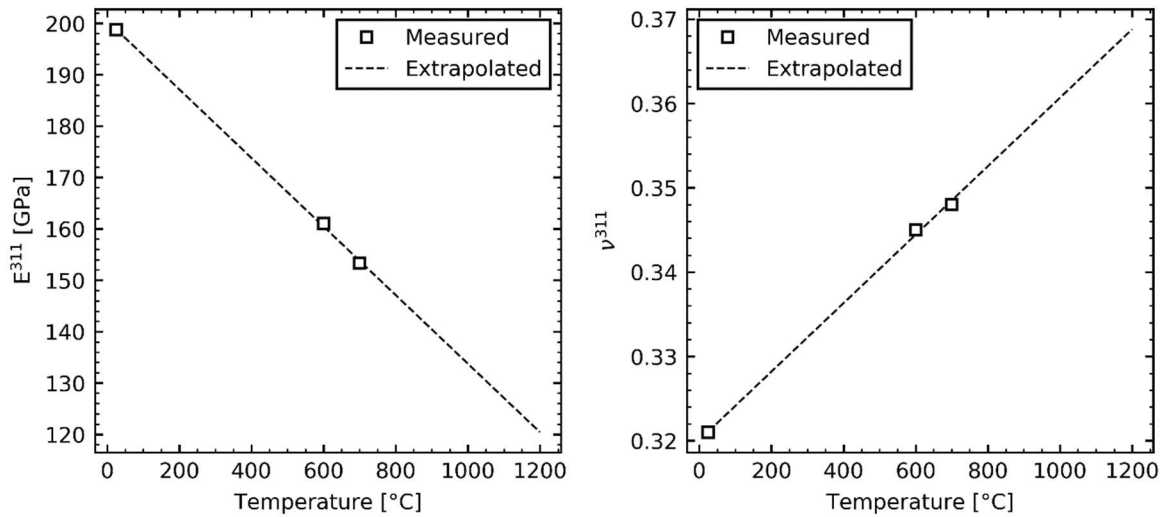


Figure 14 Results of temperature-dependent d_0 measurements.

25 6.4 Temperature-dependent X-ray Elastic Constants

26 From Wang et al. the single crystal constants c_{11} , c_{12} and c_{44} for room temperature, 600 °C and 700 °C
 27 were used to calculate the corresponding Young's modulus and Poisson ratio via the Kröner model.
 28 Afterwards, those values were used for a linear regression to extrapolate to higher temperatures as
 29 shown in **Figure 15**.

30 In **Table 2**, the single crystal constants from Wang et al., the derived Young's moduli and Poisson
 31 ratios as well as the extrapolated values used to calculate **Figure 9** are given.



32

33 **Figure 15** Calculated Young's modulus and Poisson ratio based on the singly crystal constants determined by
 34 Wang et al. [47]. Extrapolation using a linear regression.

35

36 **Table 2** Numerical values of elastic constants used for the calculation of stresses in **Figure 9**

Temperature	Wang et al. [47]			Kröner	
	c_{11} [GPa]	c_{12} [GPa]	c_{44} [GPa]	E^{311} [GPa]	ν^{311}
25 °C	243.3	156.7	117.8	198.7	0.321
600 °C	214.8	153.1	101.1	161.0	0.345
700 °C	205.2	149.3	99.3	153.3	0.348

Extrapolation for Figure 9		
Temperature	E^{311} [GPa]	ν^{311}
300 °C	180.5	0.332
900 °C	140.4	0.357
1200 °C	120.4	0.369

37

38